A&A 530, L16 (2011)
DOI: 10.1051/0004-6361/201116977

Astronomy & Astrophysics

Letter to the Editor

OH emission from warm and dense gas in the Orion Bar PDR⋆,⋆⋆

J. R. Goicoechea[1], C. Joblin[2,3], A. Contursi[4], O. Berné[5], J. Cernicharo[1], M. Gerin[6], J. Le Bourlot[7], E. A. Bergin[8], T. A. Bell[1], and M. Röllig[9]

[1] Centro de Astrobiología (CSIC/INTA), Ctra. de Torrejón a Ajalvir, km 4, 28850 Torrejón de Ardoz, Madrid, Spain
e-mail: jr.goicoechea@cab.inta-csic.es
[2] Université de Toulouse, UPS-OMP, IRAP, Toulouse, France
[3] CNRS, IRAP, 9 Av. colonel Roche, BP 44346, 31028 Toulouse Cedex 4, France
[4] Max-Planck-Institut für extraterrestrische Physik (MPE), Postfach 1312, 85741 Garching, Germany
[5] Leiden Observatory, Leiden University, PO Box 9513, 2300 RA Leiden, The Netherlands
[6] LERMA, UMR 8112 du CNRS, Observatoire de Paris, École Normale Supérieure, France
[7] Observatoire de Paris, LUTH and Université Denis Diderot, Place J. Janssen, 92190 Meudon, France
[8] Department of Astronomy, University of Michigan, 500 Church Street, Ann Arbor, MI 48109, USA
[9] I. Physikalisches Institut, Universität zu Köln, Zülpicher Str. 77, 50937 Köln, Germany

Received 29 March 2011 / Accepted 11 May 2011

ABSTRACT

As part of a far-infrared (FIR) spectral scan with *Herschel*/PACS, we present the first detection of the hydroxyl radical (OH) towards the Orion Bar photodissociation region (PDR). Five OH ($X\ ^2\Pi$; $v = 0$) rotational Λ-doublets involving energy levels out to $E_u/k \sim 511$ K have been detected (at ∼65, ∼79, ∼84, ∼119 and ∼163 μm). The total intensity of the OH lines is $\sum I(\mathrm{OH}) \simeq 5\times10^{-4}$ erg s^{-1} cm^{-2} sr^{-1}. The observed emission of rotationally excited OH lines is extended and correlates well with the high-J CO and CH^+ $J = 3$–2 line emission (but apparently not with water vapour), pointing towards a common origin. Nonlocal, non-LTE radiative transfer models including excitation by the ambient FIR radiation field suggest that OH arises in a small filling factor component of warm ($T_k \simeq 160$–220 K) and dense ($n_\mathrm{H} \simeq 10^{6-7}$ cm^{-3}) gas with source-averaged OH column densities of $\gtrsim 10^{15}$ cm^{-2}. High density and temperature photochemical models predict such enhanced OH columns at low depths ($A_\mathrm{V} \lesssim 1$) and small spatial scales (∼10^{15} cm), where OH formation is driven by gas-phase endothermic reactions of atomic oxygen with molecular hydrogen. We interpret the extended OH emission as coming from unresolved structures exposed to far-ultraviolet (FUV) radiation near the Bar edge (photoevaporating clumps or filaments) and not from the lower density "interclump" medium. Photodissociation leads to OH/H_2O abundance ratios (>1) much higher than those expected in equally warm regions without enhanced FUV radiation fields.

Key words. astrochemistry – infrared: ISM – ISM: abundances – ISM: molecules

1. Introduction

In quiescent regions irradiated by cosmic- or X-rays, the oxygen chemistry is initiated by the charge transfer from H^+ and H_3^+ to atomic oxygen, forming O^+ and OH^+. In warm environments it can also start with the reaction of atomic oxygen with $H_2(v = 0)$ to form OH. This endothermic reaction (by ∼0.08 eV) possesses an activation barrier of a few thousand K and high gas temperatures (≳400 K) are needed to produce significant OH abundances (e.g., in shocked gas). In molecular clouds exposed to strong far-ultraviolet (FUV) radiation fields, the so-called PDRs, the gas is heated to relatively high temperatures and there are also high abundances of FUV-pumped vibrationally excited molecular hydrogen $H_2^*(v = 1, 2...)$ (Hollenbach & Tielens 1997). The internal energy available in H_2^* can be used to overcome the $O(^3P) + H_2(v = 0)$ reaction barrier (see Agúndez et al. 2010, and references therein). Although not well constrained observationally, enhanced OH abundances are expected in warm PDRs.

OH is a key intermediary molecule in the FUV-illuminated gas because further reaction of OH with H_2, C^+, O, N or S^+ leads to the formation of H_2O, CO^+, O_2, NO or SO^+ respectively. Besides, OH is the product of H_2O photodissociation, the main destruction route of water vapour in the gas unshielded against FUV radiation. Observations of OH in specific environments thus constrain different chemical routes of the oxygen chemistry.

Previous observations with *KAO* and *ISO* have demonstrated that OH is a powerful tracer of the warm neutral gas in shocked gas; from protostellar outflows and supernova remnants to extragalactic nuclei (e.g., Storey et al. 1981; Melnick et al. 1987; Gonzalez-Alfonso et al. 2004). Unfortunately, the poor angular resolution (>1′) and sensitivity of the above telescopes prevented us from resolving the OH emission from interstellar PDRs.

Owing to its proximity and nearly edge-on orientation, the interface region between the Orion Molecular Cloud 1 (OMC1) and the H II region illuminated by the Trapezium cluster, the Orion Bar, is the prototypical warm PDR (with a FUV radiation field at the ionization front of $\chi \simeq 2.5\times10^4$ times the mean interstellar field in Draine units; Marconi et al. 1998). The most commonly accepted scenario is that an extended gas component, with mean gas densities n_H of 10^{4-5} cm^{-3}, causes the chemical stratification seen in the PDR (Hogerheijde et al. 1995). Most of

⋆ *Herschel* is an ESA space observatory with science instruments provided by European-led Principal Investigator consortia and with important participation from NASA.
⋆⋆ Appendix B is available in electronic form at http://www.aanda.org

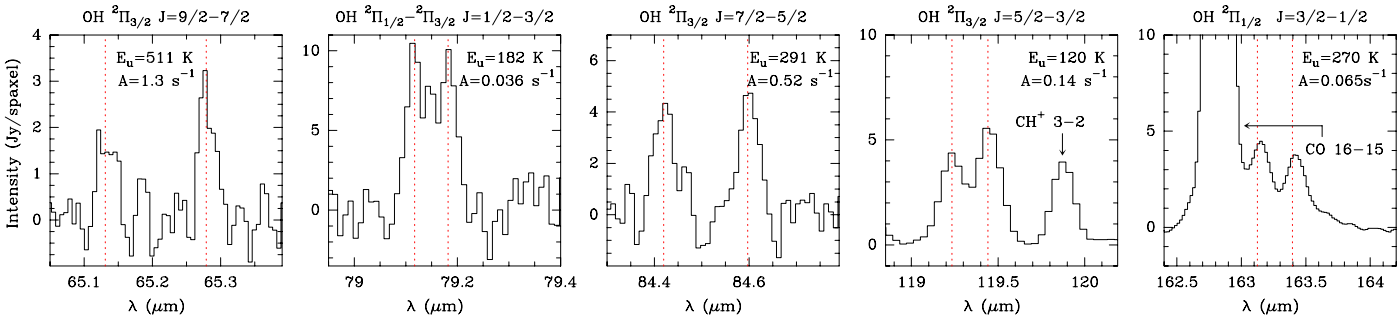

Fig. 1. OH (X $^2\Pi$; $v = 0$) rotational lines detected with *Herschel*/PACS towards the $\alpha_{2000} \simeq 5^h35^m21.9^s$, $\delta_{2000} \simeq -5°25'06.7''$ position where the higher excitation OH line peak is observed (see Fig. 2). The red dotted lines show the expected wavelength for each Λ-doublet (see Fig. B.1 in Appendix B for a complete OH rotational energy diagram). Small intensity asymmetries are observed in most OH Λ-doublets. Transition upper level energies and A_{ij} spontaneous transition probabilities are indicated.

the low-J molecular line emission arises in this extended "interclump" medium (Tielens & Hollenbach 1985; Simon et al. 1997; van der Wiel et al. 2009; Habart et al. 2010). In addition, another component of higher density clumps was introduced to fit the observed H_2, high-J CO, CO^+ and other high density and temperature tracers (Burton et al. 1990; Parmar et al. 1991; Störzer et al. 1995; van der Werf et al. 1996; Young Owl et al. 2000). Owing their small filling factor this clumpy structure would allow FUV radiation to permeate the region. The presence of dense clumps is still controversial.

In this letter we present initial results from a spectral scan of the Orion Bar taken with the PACS instrument (Poglitsch et al. 2010) on board *Herschel* (Pilbratt et al. 2010) as part of the "HEXOS" key programme (Bergin et al. 2010). PACS observations of OH lines towards young stellar objects have recently been reported by Wampfler et al. (2010). Here we present the first detection of OH towards this prototypical PDR.

2. Observations and data reduction

PACS observations were carried out on 7 and 8 September 2010 and consist of two spectral scans in Nyquist sampling wavelength range spectroscopy mode. The PACS spectrometer uses photoconductor detectors and provides 25 spectra over a $47'' \times 47''$ field-of-view resolved in 5×5 spatial pixels ("spaxels"), each with a size of $\sim 9.4'' \times 9.4''$ on the sky. The measured width of the spectrometer point-spread function (PSF) is relatively constant at $\lambda \lesssim 125\,\mu$m but it increases above the spaxel size for longer wavelengths. The resolving power varies between $\lambda/\Delta\lambda \sim 1000$ (R1 grating order) and ~5000 (B3A). The central spaxel was centred at α_{2000}: $5^h35^m20.61^s$, δ_{2000}: $-5°25'14.0''$ target position. Observations were carried out in the "chop-nodded" mode with the largest chopper throw of 6 arcmin. Nominal capacitances (0.14 pF) were used. The integration time was 3.2 h for the 1342204117 observation (B2B and R1) and 2.7 h for the 1342204118 observation (B3A and R1). The data were processed with HIPE using a pipeline upgraded with a spectral flatfield algorithm that reduces the spectral fringing seen in the Nyquist-sampled wavelength spectra of bright sources. Figure 1 shows the resulting OH lines towards the OH emission peak and Fig. 3 shows the intensities measured in each of the 25 spaxels for several lines of OH, CO, CH^+, H_2O and [N II]. In order to better sample the PSF and obtain accurate line intensities to be reproduced with our models, we fit the OH emission averaged over several adjacent spaxels in Sect. 4 (see also Appendix A).

3. Results

Of all the observed OH lines only the ground-state lines at ~119 μm show widespread bright emission at all positions. The ~119 μm lines mainly arise from the background OMC1 complex (the same applies to most ground-state lines of other species). Figure 2 shows the spatial distribution of the rotationally excited OH $^2\Pi_{3/2}$ $J = 7/2 \rightarrow 5/2$ lines at ~84 μm (E_u/k = 291 K) superimposed over the CO $J = 6$–5 peak brightness temperature (colour image from Lis et al. 1998) and over the brightest H_2^* $v = 1$–0 $S(1)$ line emission regions (white contours from Walmsley et al. 2000). The emission from the other OH Λ-doublets at ~79 and ~163 μm (see Fig. B.2 in Appendix B) displays a similar spatial distribution that follows the "bar" morphology peaking near the H_2^* $v = 1$–0 $S(1)$ bright emission region and then decreases with distance from the ionization front (note that H_2^* shows lower level extended emission with small-scale structure in the entire observed field; van der Werf et al. 1996). The excited OH spatial distribution, however, does not follow the CO $J = 6$–5 emission maxima, which approximately trace the gas temperature in the extended "interclump" component.

Figure 1 shows the detected OH Λ-doublets (at ~65, ~79, ~84, ~119 and ~163 μm) towards the position where the higher excitation OH lines peak. The total intensity of the observed FIR lines is $\sum I(\mathrm{OH}) \simeq 5 \times 10^{-4}$ erg s^{-1} cm^{-2} sr^{-1}. All OH doublets appear in emission, with intensity asymmetry ratios up to 40% (one line of the Λ-doublet is brighter than the other).

Note that the upper energy level of the $^2\Pi_{3/2}$ $J = 9/2 \rightarrow 7/2$ transition at ~65 μm lies at $E_u/k \sim 511$ K. The critical densities ($n_{\rm cr}$) of the observed OH transitions are high, $n_{\rm cr} \gtrsim 10^8$ cm^{-3}. For much lower gas densities, and in the presence of strong FIR radiation fields, most lines would have been observed in absorption, especially those in the $^2\Pi_{3/2}$ ladder (Goicoechea & Cernicharo 2002). Hence, the observed OH lines must arise in an widespread component of warm and dense gas.

Although our PACS observations do not provide a fully sampled map, the line emission observed in the 25 spaxels can be used to carry out a first-order analysis on the spatial correlation of different lines (neglecting perfect PSF sampling, line opacity and excitation effects). Except for the OH ground-state lines at ~119 μm (that come from the background OMC1 cloud), we find that the rotationally excited OH lines correlate well with the high-J CO and CH^+ emission but, as expected, they do not correlate with the ionized gas emission. Figure 3 (*lower panel*) compares the observed OH ~84.597 μm line intensities with those of CO $J = 21$–20 ($E_u/k \sim 1276$ K), CH^+ $J = 3$–2

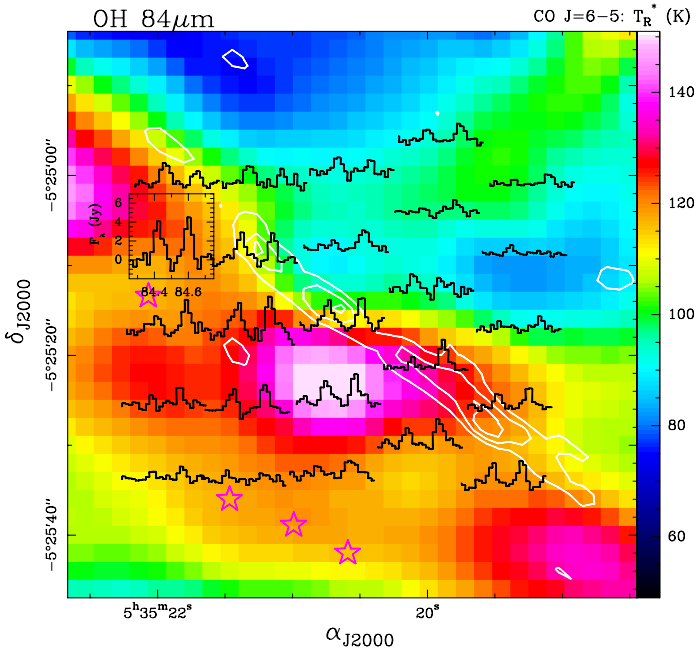

Fig. 2. PACS rotationally excited OH $^2\Pi_{3/2}$ $J = 7/2 \rightarrow 5/2$ lines at ~84 μm (E_u/k = 291 K) overlaid on the distribution of the CO J = 6–5 peak brightness temperature (colour image) observed with the CSO telescope at ~11″ resolution (Lis et al. 1998). White contours show the brightest regions of H_2^* v = 1–0 $S(1)$ emission (Walmsley et al. 2000). Lower intensity H_2^* extended emission is present in the entire field (van der Werf et al. 1996). Violet stars shows the position of the $H^{13}CN$ J = 1–0 clumps deeper inside the Bar (Lis & Schilke 2003). Note the decrease of OH line intensity with distance from the ionization front.

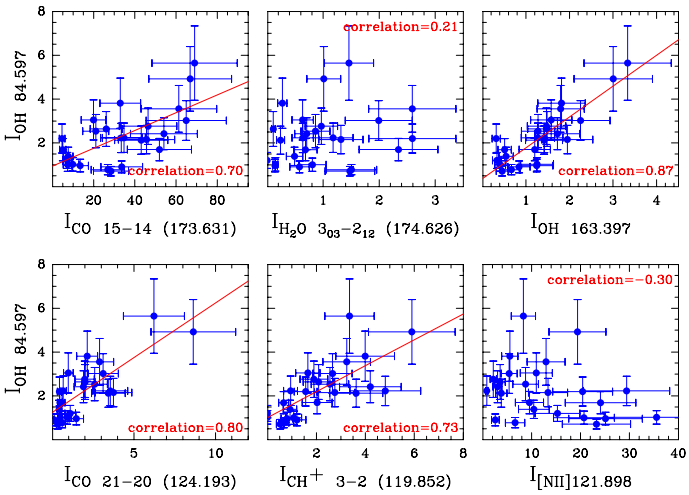

Fig. 3. Line intensity spatial correlations between the OH $^2\Pi_{3/2}$ $J = 7/2^- \rightarrow 5/2^+$ line at 84.597 μm and lines from other species. Intensities are in units of 10^{-5} erg cm^{-2} s^{-1} sr^{-1} and wavelengths are in μm.

(E_u/k ~ 240 K) and [N II]121.891 μm (all observed with a similar PSF) and also with the CO J = 15–14 (E_u/k ~ 663 K), H_2O 3_{03}–2_{12} (E_u/k ~ 163 K) and OH ~ 163.397 μm lines (*upper panel*). This simple analysis suggests that the excited OH, high-J CO and CH^+ J = 3–2 lines arise from the same gas component. It also shows that the emission from different excited OH lines is well correlated, while the OH and H_2O emission is not (within the PSF sampling caveats).

4. OH column density determination

Determining the OH level populations is no trivial excitation problem. In addition to relatively strong asymmetries in the collisional rate coefficients[1] between each Λ-doubling component (Offer & Van Dishoeck 1992), radiative and opacity effects (pumping by the ambient IR radiation field and line trapping) can play a significant role if the gas density is much lower than n_{cr}. Here we use a nonlocal and non-LTE code that treats both the OH line and continuum radiative transfer (see appendix in Goicoechea et al. 2006). The continuum measured by PACS and SPIRE in the region (Arab et al., in prep.) can be approximately reproduced by a modified blackbody with a colour temperature of ~55 K and a opacity dependence of ~$0.05(100/\lambda)^{1.75}$ (see Lis et al. 1998). Our calculations include thermal, turbulent, and opacity line broadening with a turbulent velocity dispersion of σ = 1.0 km s^{-1} and $FWHM = 2.355 \times \sigma$ (see e.g., the linewidths measured by Hogerheijde et al. 1995). A grid of single-component models for different N(OH), gas temperatures, densities and beam filling factors were run. The best fit model was found by minimizing the "χ^2-value" (see Appendix A for its definition).

From the excitation models we conclude that the high $I(65.279)/I(84.596) \simeq 0.3$ and $I(65.132)/I(84.420) \simeq 0.5$ intensity ratios in the $^2\Pi_{3/2}$ ladder can only be reproduced if the gas is dense, at least $n_H = n(H) + 2n(H_2)$ of a few 10^6 cm^{-3}. In addition, no model is able to produce even a crude fit to the data if one assumes the average molecular gas temperature ($T_k \simeq 85$ K) in the lower density "interclump" medium (Hogerheijde et al. 1995). In the $^2\Pi_{1/2}$ ladder, the intensity of the ~163 μm lines is sensitive to the FIR radiation field in the region through the absorption of FIR dust continuum photons in the OH ~34 and ~53 μm cross-ladder transitions ($^2\Pi_{3/2}$–$^2\Pi_{1/2}$ $J = 3/2 \rightarrow 5/2$ and $J = 3/2 \rightarrow 3/2$ respectively). However, the ~163 μm lines in the Orion Bar are not particularly strong and the OH ~34 and ~53 μm lines are not present in the ISO spectra, thus FIR pumping does not dominate the OH excitation. All in all, the best model is found for a source of high density ($n_H \lesssim 10^7$ cm^{-3}) and warm gas temperatures (T_k = 160–220 K). This temperature lies in between the ~600 K derived in the H_2 emitting regions (Allers et al. 2005) and the ~150 K derived from NH_3 lines (Batrla & Wilson 2003) near the ridge of dense and cooler $H^{13}CN$ clumps ($T_k \simeq 50$ K; Lis & Schilke 2003). In our simple model, the best fit is obtained for a source of small filling factor ($\eta \simeq 10\%$) with a source-averaged OH column density of $\gtrsim 10^{15}$ cm^{-2} (see Appendix A).

5. OH chemistry and line emission origin

We used the Meudon PDR code (Le Petit et al. 2006; Goicoechea & Le Bourlot 2007) to estimate the OH column density in a slab of gas at different densities (n_H from 5×10^4 to 10^7 cm^{-3}). The adopted FUV radiation field, $\chi = 10^4$, roughly corresponds to the attenuation of the FUV field at the ionization front by a column density of $N_H \simeq 10^{21}$ cm^{-2} in a $n_H \simeq 10^4$ cm^{-3} medium. This attenuation is equivalent to a spatial length of

[1] We used collision rate coefficients of OH with *para*- and *ortho*-H_2 from Offer & van Dishoeck (1992) and Offer et al. (1994). Strong differences in the intensity of each OH Λ-doublet component due to asymmetries in the collisional rates between OH and *para*-H_2 were predicted (e.g., $I(84.597)/I(84.420) > I(119.441)/I(119.234) > 1$). Asymmetries are significantly reduced when collisions with *ortho*-H_2 are included (i.e., in the warm gas) and when FIR radiative pumping plays a role. We assume that the H_2 *ortho*-to-*para* ratio is thermalized to the gas temperature, e.g., ~1.6 at 100 K and ~2.9 at 200 K.

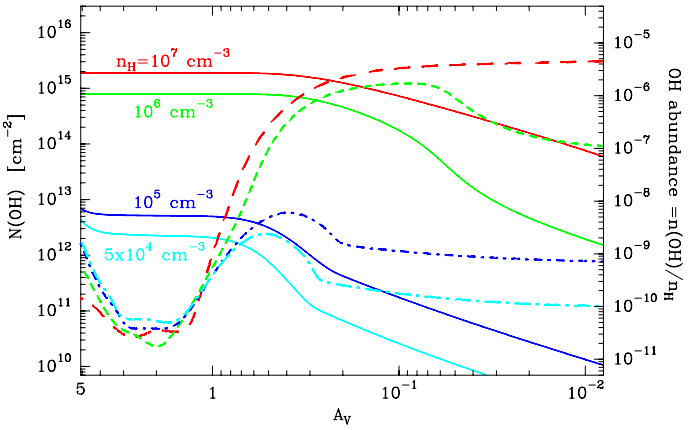

Fig. 4. Gas-phase PDR models of a FUV-illuminated slab ($\chi = 10^4$) of gas with different densities: $n_H = 10^7$, 10^6, 10^5 and 5×10^4 cm^{-3}. OH column densities are shown as continuous curves (left axis) while OH abundances, n(OH)/n_H, are shown as dashed curves (right axes).

$\sim 10^{17}$ cm, consistent with the observed decrease of excited OH emission with projected distance from the ionization front (see Fig. 2). Given the high gas temperature, FUV field and moderate grain temperature ($T_{gr} \sim$ 70–100 K) in the regions traced by FIR OH, CO and CH^+ lines, we neglected molecule freeze-out and ice desorption (which are important deeper inside at $A_V \gtrsim 3$; Hollenbach et al. 2009). In our models OH is a surface tracer that reaches its peak abundance at $A_V \lesssim 1$ (Fig. 4) where OH formation is driven by the endothermic reaction $O(^3P) + H_2 \rightarrow OH + H$, slightly enhanced by the $O(^3P) + H_2^*$ reaction (included in our models; see Agúndez et al. 2010). Gas temperatures around ~1000–500 K are predicted near the slab surface at $A_V = 0.01$ and around ~100 K at $A_V \gtrsim 1$. In these H/H_2 transition layers where the OH abundance peaks, the electron density is still high ($\lesssim$[C^+/H] n_H) and hydrogen is not fully molecular, with $f(H_2) = 2n(H_2)/[n(H) + 2n(H_2)] \simeq 0.5$. In general, the higher the gas temperature where enough H_2 has formed, the higher the predicted OH abundance.

In the $A_V \lesssim 1$ layers, OH destruction is dominated by photodissociation ($OH + h\nu \rightarrow O + H$) and to a lesser extent, by reactions of OH with H_2 to form H_2O (only when the gas temperature and density are very high). Water vapour photodissociation ($H_2O + h\nu \rightarrow OH + H$) in the surface layers limits the H_2O formation and leads to OH/H_2O abundance ratios (>1), much higher than those expected in equally warm regions without enhanced FUV radiation fields (e.g. in C-shocks). The lack of apparent correlation between the excited OH and H_2O 3_{03}-2_{12} lines (see Fig. 3) and the absence of high excitation H_2O lines in the PACS spectra (only weak H_2O 2_{21}–2_{12}, 2_{12}–1_{01} and 3_{03}–2_{12} lines are clearly detected) suggests that the bulk of OH and H_2O column densities arise from different depths.

As the temperature decreases inwards, the gas-phase production of OH also decreases. The spatial correlation between excited OH, CH^+ $J = 3$–2 and high-J CO lines is a good signature of their common origin in the warm gas at low A_V depths.

Our PDR models predict OH column densities in the range $\sim 10^{12}$ cm^{-2} to $\sim 10^{15}$ cm^{-2} at $A_V \lesssim 1$ for gas densities between $n_H = 5 \times 10^4$ and 10^7 cm^{-3} respectively. Hence, even if we take into account possible inclination effects, high density and temperature models produce OH columns closer to the values derived in Sect. 4 just from excitation considerations (note that a precise determination of the gas density would require knowing the collisional rate coefficients of OH with H atoms and electrons). The OH abundance in these dense surface layers is of the order of $\approx 10^{-6}$ with respect to H nuclei. However, optical depths of $A_V \lesssim 1$ correspond to spatial scales of only $\sim 10^{15}$ cm (i.e., much smaller than the $H^{13}CN$ clumps detected by Lis & Schilke 2003, deeper inside the cloud), but we detect extended OH emission over $\sim 10^{17}$ cm scales. Therefore, we have to conclude that the observed OH emission arises from a small filling factor ensemble of unresolved structures that are exposed to FUV radiation (overdense clumps or filaments). Note that owing to the lower grain temperature compared to the gas, the expected FIR continuum emission from these clumps will still be below the continuum levels observed by *Herschel*/PACS.

The minimum size of the dense clumps is $\sim 10^{15}$ cm (from OH photochemical models) with a maximun size of $\sim 10^{16}$ cm (from the inferred beam dilution factor). Both correspond to $\lesssim$0.2″–2″ at the distance of Orion. As an example, H_2 photoevaporating clumps of $\sim 10^{16}$ cm size have been unambiguously resolved towards S106 PDR Noel et al. (2005). However, higher angular resolution observations (e.g., with 8–10 m telescopes) are needed to resolve smaller H_2 clumps from the H_2 interclump emission in the Orion Bar.

If the observed FIR OH line emission does not arise from such a high density gas component, a different non-thermal excitation mechanism able to populate the OH $^2\Pi_{3/2}$ $J = 9/2$ and 7/2 levels would be needed. Two alternative scenarios can be explored, at least qualitatively. First, OH molecules produced by H_2O photodissociation are expected to form mostly in the ground electronic and vibrational state but in unusually high energy $J > 70/2$ levels (a few thousands K!; van Harrevelt & van Hemer 2000). Nevertheless, they will cascade down radiatively to lower energy rotational ladders extremely rapidly. Although very excited suprathermal OH $J \simeq$ 70/2–15/2 lines have been reported towards the HH 211 outflow and were interpreted as H_2O photodissociation (Tappe et al. 2008), we did not find any of them in the SWS or in the IRS spectra of the Orion Bar (taken and processed by us from the ISO and *Spitzer* basic calibrated data archives). Besides, even if photodissociation is the main H_2O destruction mechanism in the $A_V \lesssim 1$ warm layers, this is not the main production pathway of OH (the $O(^3P) + H_2$ reaction dominates).

Second, experiments and quantum calculations suggest that reaction of $O(^3P)$ atoms with $H_2^*(v = 1)$ can produce significant OH in the $v = 1$ vibrationally excited state, with OH($v = 1$)/OH($v = 0$) population ratios $\gtrsim$1 for moderate kinetic energies ($\gtrsim$0.05–0.1 eV; e.g., Balakrishnan 2004). Complementarily, absorption of near- and mid-IR photons (from the continuum or from bright overlapping H_2^* and ionic lines) can also pump OH to the $v = 1$ state. In both cases, subsequent de-excitation through the $v = 1$–0 rotation-vibration band at ~2.80 μm would populate the OH($v = 0$) rotationally excited levels that we observe with PACS. However, the OH $v = 1$–0 band at ~2.80 μm is not present in the ISO/SWS spectra. Even assuming that the $O(^3P)$+$H_2^*(v = 1)$ reaction only forms OH($v = 1$), significant gas column densities at very hot temperatures ($T_k \sim 2000$ K) will be needed to match the observations if $n_H \simeq 10^{4-5}$ cm^{-3}. Studying the OH vibrationally-pumping mechanism quantitatively is beyond the scope of this work but these chemical and pumping effects could contribute to the excitation of FIR OH lines in lower density gas.

Different scenarios for the origin and nature of photoevaporating clumps have been proposed (Gorti & Hollenbach 2002), but without a more precise determination of their sizes and densities it is hard to conclude on any of them. Subarcsec resolution

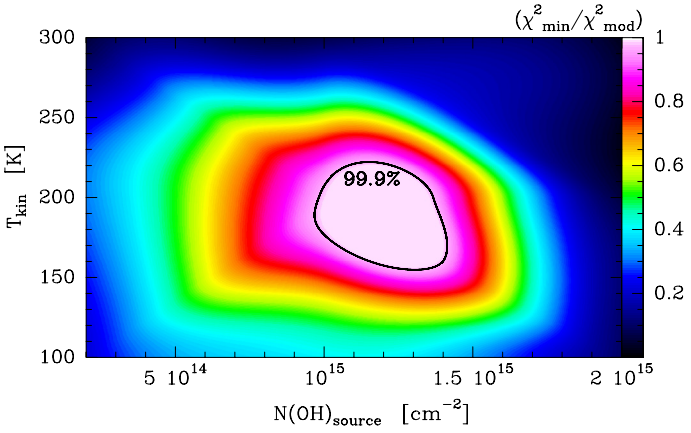

Fig. A.1. $\chi^2_{min}/\chi^2_{mod}$ as a function of T_k and N(OH) for a grid of models with $n_H = 10^7$ cm^{-3} and $\eta = 0.1$. The set of parameters giving the minimum χ^2-values with a confidence level of 99.9% are shown.

Table A.1. PACS OH line intensities towards the Orion Bar PDR[a].

λ (μm)	OH transition	I_{obs} (σ_{obs}) ($\times 10^{-5}$ erg s^{-1} cm^{-2} sr^{-1})
119.441	$^2\Pi_{3/2}$ $J = 5/2^+$–$3/2^-$	10.09 (0.21)
119.234	$^2\Pi_{3/2}$ $J = 5/2^-$–$3/2^+$	9.44 (0.21)
84.597	$^2\Pi_{3/2}$ $J = 7/2^-$–$5/2^+$	4.07 (0.79)
84.420	$^2\Pi_{3/2}$ $J = 7/2^+$–$5/2^-$	2.38 (0.91)
163.396	$^2\Pi_{1/2}$ $J = 3/2^-$–$1/2^+$	1.34 (0.17)
163.015	$^2\Pi_{1/2}$ $J = 3/2^+$–$1/2^-$	2.74 (0.16)
79.179	$^2\Pi_{1/2}$-$^2\Pi_{3/2}$ $J = 1/2^+$–$3/2^-$	9.17 (1.30)
79.115	$^2\Pi_{1/2}$-$^2\Pi_{3/2}$ $J = 1/2^-$–$3/2^+$	9.65 (1.54)
65.279	$^2\Pi_{3/2}$ $J = 9/2^+$–$7/2^-$	1.02 (0.49)
65.131	$^2\Pi_{3/2}$ $J = 9/2^-$–$7/2^+$	1.32 (0.54)

Notes. [(a)] Near the OH emission peak: $\alpha_{2000} \simeq 5^h35^m21.9^s$, $\delta_{2000} \simeq -5°25'06.7''$.

observations of OH gas-phase products, e.g., direct observation of CO^+ or SO^+ clumps with *ALMA*, will help us to assay the clumpy nature of the Orion Bar in the near future.

Acknowledgements. PACS has been developed by a consortium of institutes led by MPE (Germany) and including UVIE (Austria); KU Leuven, CSL, IMEC (Belgium); CEA, LAM (France); MPIA (Germany); INAF-IFSI/OAA/OAP/OAT, LENS, SISSA (Italy); IAC (Spain). We thank Darek Lis and Malcolm Walmsley for providing us their CO J = 6–5 and H_2^* 1–0 S(1) maps. We also thank Emilie Habart, Bart Vandenbussche and Pierre Royer for useful discussions and the referee for his/her constructive report. We thank the Spanish MICINN for funding support through grants AYA2006-14876, AYA2009-07304 and CSD2009-00038. J.R.G. is supported by a Ramón y Cajal research contract. We acknowledge the use of the LAMDA data base (Schöier et al. 2005).

Appendix A: χ^2 analysis and intensity extraction

The best-fit OH radiative transfer model was obtained by finding the minimum χ^2-value defined as

$$\chi^2 = \frac{1}{n-p}\sum_{i=1}^{n}\left(\frac{I^i_{obs} - I^i_{mod}}{\sigma^i_{obs}}\right)^2, \quad (A.1)$$

where n is the number of observed OH lines, p is the number of free parameters in the fit, I^i_{obs} and I^i_{mod} are the observed and modelled line integrated intensities, and σ^i_{obs} is the 1σ uncertainty of I^i_{obs}. Therefore, we fit absolute intensity values and not line intensity ratios. Figure A.1 shows the best grid of radiative transfer models with a density of $n_H = 10^7$ cm^{-3} and a beam filling factor $\eta = 0.1$, defined as $\eta = \frac{\Omega_s}{\Omega_s+\Omega_{PSF}}$, where Ω_s and Ω_{PSF} are the sky solid angles subtended by the source and by the PACS PSF respectively. Figure A.1 shows the best source-averaged OH column densities, where $N(OH)_{beam} \approx \eta \times N(OH)_{source}$.

The list of OH line intensities around the position where the higher excitation OH lines peak is shown in Table A.1. In order to better sample the spectrometer PSF in these extended emission observations, the OH line intensities were computed by co-adding the measured fluxes over four adjacent spaxels (the [3,4], [3,3], [2,4] and [2,3]). Owing to the broader PSF width at long wavelengths, the entire array was used to extract the OH ~ 163 μm line intensities.

References

Agúndez, M., Goicoechea, J. R., Cernicharo, J., et al. 2010, ApJ, 713, 662
Allers, K. N., Jaffe, D. T., Lacy, J. H., et al. 2005, ApJ, 630, 368
Balakrishnan, N. 2004, JChPh, 121, 6346
Batrla, W., & Wilson, T. L. 2003, A&A, 408, 231
Bergin, E. A., Phillips, T. G., Comito, C., et al. 2010, A&A, 521, L20
Burton, M. G., Hollenbach, D. J., & Tielens, A. G. G. M. 1990, ApJ, 365, 620
Goicoechea, J. R., & Cernicharo, J. 2002, ApJ, 576, L77
Goicoechea, J. R., & Le Bourlot, J. 2007, A&A, 467, 1
Goicoechea, J. R., Pety, J., Gerin, M., et al. 2006, A&A, 456, 565
González-Alfonso, E., Smith, H. A., Fischer, J., & Cernicharo, J. 2004, ApJ, 613, 247
Gorti, U., & Hollenbach, D. 2002, ApJ, 573, 215
Habart, E., Dartois, E., Abergel, A., et al. 2010, A&A, 518, L116
Hogerheijde, M. R., Jansen, D. J., & van Dishoeck, E. F. 1995, A&A, 294, 792
Hollenbach, D. J., & Tielens, A. G. G. M. 1997, ARA&A, 35, 179
Hollenbach, D., Kaufman, M. J., Bergin, E. A., & Melnick, G. J. 2009, ApJ, 690, 1497
Marconi, A., Testi, L., Natta, A., & Walmsley, C. M. 1998, A&A, 330, 696
Melnick, G. J., Genzel, R., & Lugten, J. B. 1987, ApJ, 321, 530
Noel, B., Joblin, C., Maillard, J. P., & Paumard, T. 2005, A&A, 436, 569
Le Petit, F., Nehmé, C., Le Bourlot, J., & Roueff, E. 2006, ApJS, 164, 506
Lis, D. C., & Schilke, P. 2003, ApJ, 597, L145
Lis, D. C., Serabyn, E., Keene, J., et al. 1998, ApJ, 509, 299
Offer, A. R., & van Dishoeck, E. F. 1992, MNRAS, 257, 377
Offer, A. R., van Hemert, M. C., & van Dishoeck, E. F. 1994, J. Chem. Phys., 100, 362
Parmar, P. S., Lacy, J. H., & Achtermann, J. M. 1991, ApJ, 372, L25
Pilbratt, G. L., Riedinger, J. R., Passvogel, T., et al. 2010, A&A, 518, L1
Poglitsch, A., Waelkens, C., Geis, N., et al. 2010, A&A, 518, L2
Schöier, F. L., van der Tak, F. F. S., van Dishoeck, E. F., & Black, J. H. 2005, A&A, 432, 369
Simon, R., Stutzki, J., Sternberg, A., & Winnewisser, G. 1997, A&A, 327, L9
Störzer, H., Stutzki, J., & Sternberg, A. 1995, A&A, 296, L9
Storey, J. W. V., Watson, D. M., & Townes, C. H. 1981, ApJ, 244, L27
Tappe, A., Lada, C. J., Black, J. H., & Muench, A. A. 2008, ApJ, 680, L117
Tielens, A. G. G. M., & Hollenbach, D. 1985, ApJ, 291, 722
van der Werf, P., Stutzki, J., Sternberg, A., & Krabbe, A. 1996, A&A, 313, 633
van der Wiel, M. H. D., van der Tak, F. F. S., Ossenkopf, V., et al. 2009, A&A, 498, 161
van Harrevelt, R., & van Hemert, M. C. 2000, J. Chem. Phys., 112, 5787
Walmsley, C. M., Natta, A., Oliva, E., & Testi, L. 2000, A&A, 364, 301
Wampfler, S. F., Herczeg, G. J., Bruderer, S., et al. 2010, A&A, 521, L36
Young Owl, R. C., Meixner, M. M., Wolfire, M., Tielens, A. G. G. M., & Tauber, J. 2000, ApJ, 540, 886

Appendix B: Figures

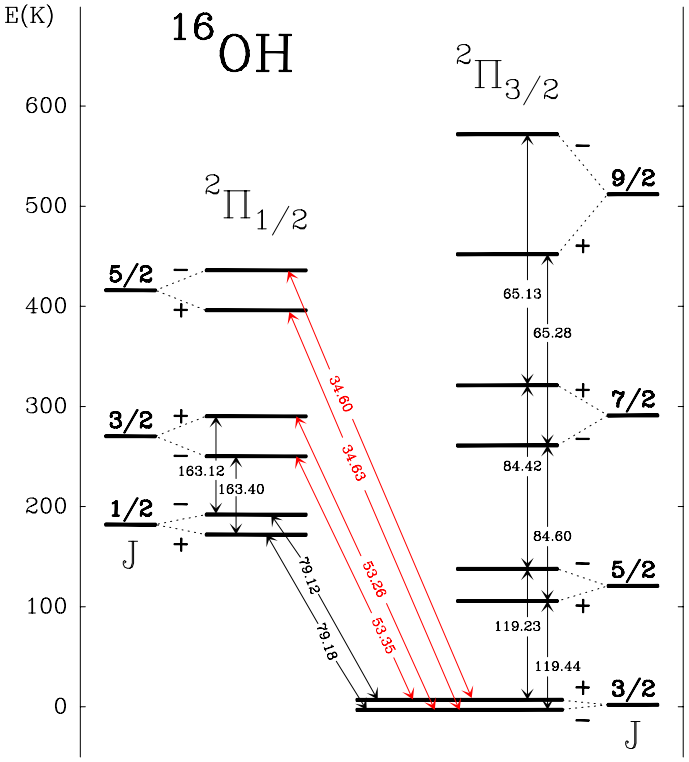

Fig. B.1. Rotational energy diagram of ^{16}OH showing the lines detected by *Herschel*/PACS (in microns). Detected transitions are shown in black while other pumping transitions discussed in the text are shown in red. OH $^2\Pi_{3/2}$ and $^2\Pi_{1/2}$ rotational ladders are produced by the spin-orbit interaction, while the Λ-doubling splitting of each rotational level is produced by the nuclei rotation and the unpaired electron motion. The Λ-doubling splitting has been enhanced for clarity. Hyperfine structure is not shown.

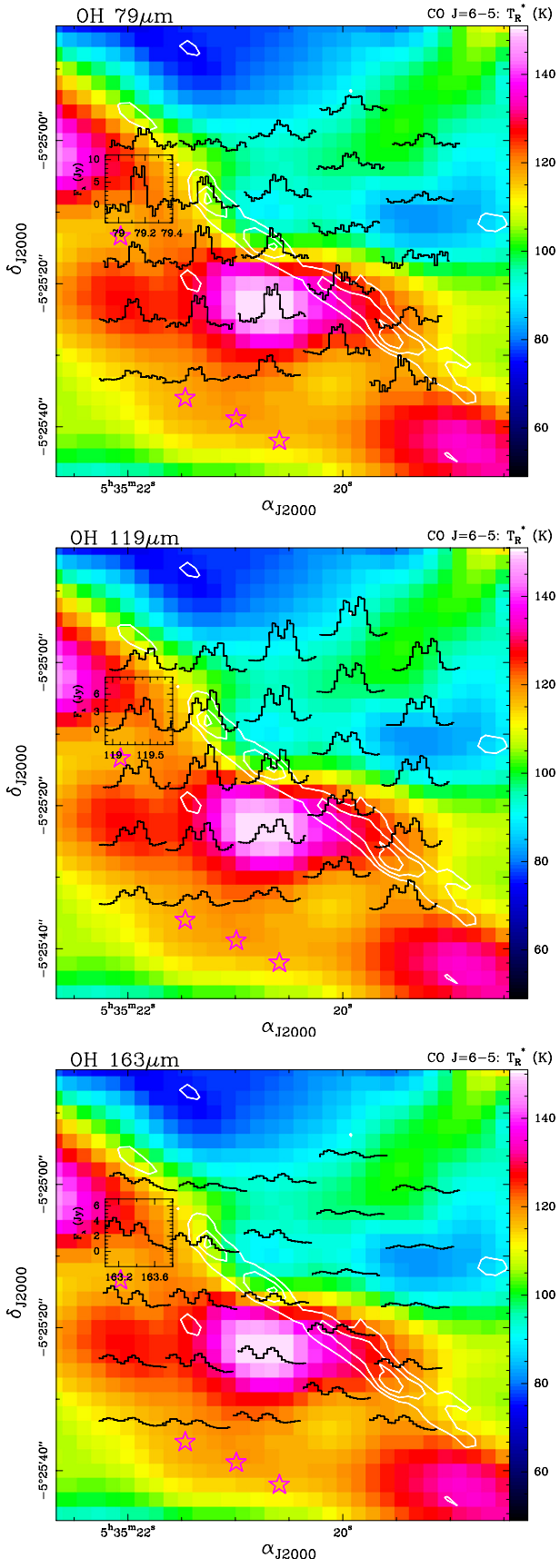

Fig. B.2. Same as Fig. 2 for the OH $^2\Pi_{1/2}$–$^2\Pi_{3/2}$ $J = 1/2 \rightarrow 3/2$ cross-ladder lines at ~79 μm, the OH $^2\Pi_{3/2}$ $J = 5/2 \rightarrow 3/2$ ground-state lines at ~119 μm, and the OH $^2\Pi_{1/2}$ $J = 3/2 \rightarrow 1/2$ excited lines at ~163 μm. Note the decrease of OH line intensity with distance from the ionization front.